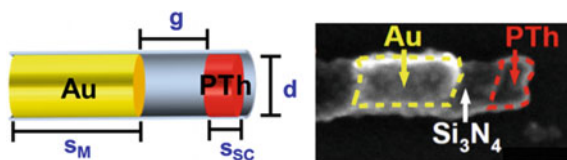


## Chapter 2

# 1D Nanowire Synthesis: Extending the OWL Toolbox with Semiconductors to Explore Plasmon-Exciton Interactions in the Form of Long-Range Optical Nanoscale Rulers



## 2.1 Introduction

Förster resonant energy transfer (FRET) between molecular fluorophores has been commonly used to measure the distance between molecular entities within biological systems [1, 2]. The technique, however, is limited to the sub-10 nm range [1, 2]. To access longer distances, “rulers” based upon plasmonic architectures have been developed. Indeed, techniques that focus on surface-enhanced Raman-scattering (SERS, surface-to-molecule, sub-20 nm) [3], nanoparticle-based surface energy transfer (surface-to-molecule, sub-50 nm) [4–6] photoluminescence (PL) lifetime (surface-to-molecule, sub-50 nm) [6] and optical coupling between plasmonic dimers (particle-to-particle, sub-100 nm) [7–13] have all been developed for measuring distances on the nanoscale. These structures are often referred to as optical rulers and have strengths and weaknesses depending upon intended application. They are either limited in terms of distance that can be measured or the requirement of two metal particles.

---

Portions of this chapter have been published in *Nano Letters* 13 (5), 2270 (2013).

Co-authors of this work: Gilles R. Bourret, Martin Blaber, Chad M. Shade, George C. Schatz, Chad A. Mirkin.

Copyright 2013 American Chemical Society.

The structures that utilize plasmonic particle-fluorophore pairs are quite interesting because they provide a variety of physical parameters that can be influenced by the juxtaposition of these two types of materials [14]. For example, because of their intense and highly localized electromagnetic fields, plasmonic nanostructures can significantly enhance important processes, including photo- and electro-luminescence [15], photoelectric response [16–18] and photocatalytic activity [16, 19–21]. In particular, plasmonic nanoantennas can be used to modulate the rate [22, 23], intensity [24–26] direction [27], polarization [28–32] and spectral shape [33–36] of the spontaneous emission of neighboring luminescent emitters. Since the emission of a strongly-coupled fluorescent/plasmonic pair carries characteristics from both components, such structures are often referred to as plasmonophores [14]. Since the plasmon-exciton interaction governing the plasmonophore emission is affected by: (i) the overlap of both the absorption and the emission bands of the fluorescent material with the surface plasmon resonance (SPR) of the plasmonic structure, (ii) the near-field intensity generated by the plasmonic construct, and (iii) the distance between the two structures, one can therefore design efficient optical rulers by using specific pairs of plasmonic and luminescent nanostructures [5, 6, 37]. Indeed, the distance-dependent plasmonic modulations of both the PL lifetime and intensity of fluorophores have been measured and used to construct medium-range nanoscale rulers (i.e. sub-50 nm) [5, 6, 37]. However, the effect of distance on the plasmon-induced modification of the PL spectral shape of luminescent emitters has never been studied. Herein, we take advantage of the strong plasmonic fields generated by gold nanorods to develop the first long-range “plasmonophore rulers” (valid up to 100 nm) based on the distance-dependent modulation of the emission shape of a luminescent object by a resonant plasmonic nanorod. In addition, we use On-Wire Lithography (OWL) to systematically study the optical responses of plasmonic nanostructures separated by nanoscopic distances from fluorescent semiconducting materials. This geometry, easily accessible by OWL, provides for a test-bed to study the influence of the plasmonic structure on the PL of the neighboring fluorescent materials. A theoretical model of the results is presented which both quantitatively describes the results and shows how plasmon enhancements are responsible for the observed variation of lineshape with gap size, rod length and other structural parameters.

OWL was invented in 2005 for synthesizing one-dimensional arrays of metal nanorods with deliberately designed nano- and micronscale gaps (Fig. 2.1) [38–41]. Recently, we developed a strategy for making structures with diameters as small as 35 nm [42]. This technique involves the sequential electrodeposition of conductive materials within porous anodic aluminum oxide (AAO) membranes to generate striped nanowires with segment lengths ranging from one nanometer to a few microns. OWL can be used to generate solution-processable ordered arrays (as opposed to surface patterning techniques such as e-beam lithography) [43] that are stable in the solid-state and can be made of different materials. The versatility of OWL has allowed for the fabrication of a wide variety of structures that have led to advances in organic electronics [44, 45], SERS, [46–49] plasmonics [42], and biosensing [46–49]. Thus far, OWL has been primarily used to fabricate metal

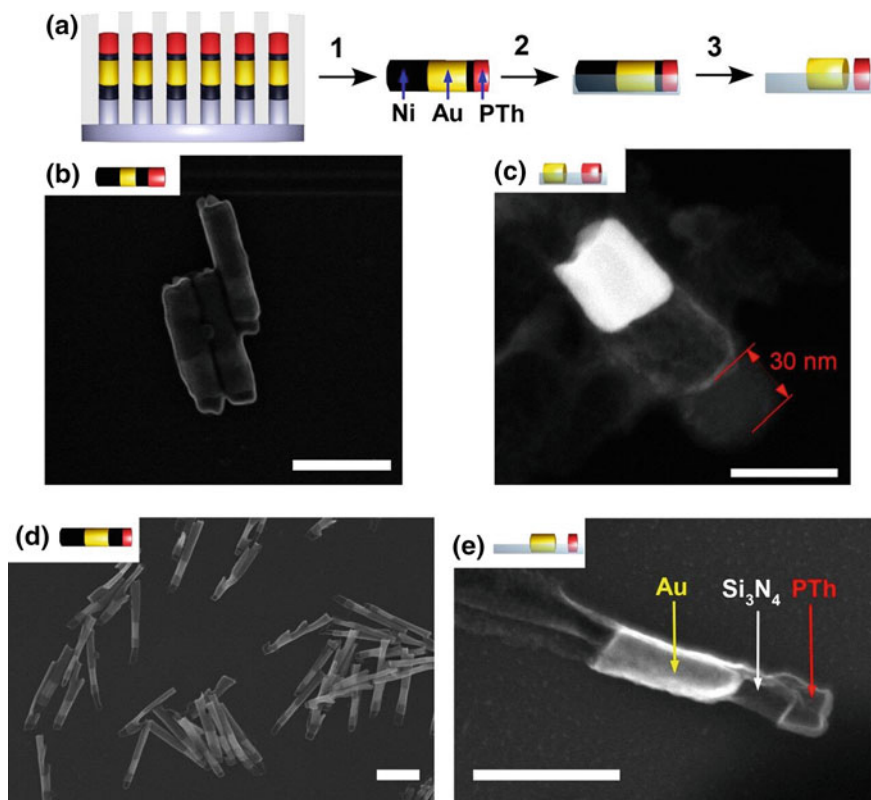


**Fig. 2.1** OWL process. **a** (1) Release of the multi-segmented nanorods by etching the AAO template and the metal backing. (2) Filtration on a porous membrane and sputtering of a thin  $\text{Si}_3\text{N}_4$  backing layer (light blue). (3) Chemical etching of the sacrificial layer (Ni, shown in black). **b–e** Electron microscopy images of the structures made using OWL. **b** SEM image of Ni-Au-Ni-PTh rods (40 nm diameter) before etching, scale bar: 200 nm. **c** Z-contrast STEM image of the Au-gap-PTh structure made by etching the structure shown in B, scale bar: 50 nm. **d** SEM image of Ni-Au-Ni-PTh rods (70 nm diameter) before etching, scale bar: 400 nm. **e** SEM image of the Au-gap-PTh structure made by etching the structure shown in D, scale bar: 200 nm (Color figure online)

nanostructures (i.e. Pt, Au, Ag and Ni), mostly because they are easily plated from solution and often form stable nanostructures [38, 41, 42, 47].

This chapter describes the first synthesis of plasmonic metal and luminescent organic polymer nanorod dimers based upon OWL, and we explore how such structures can be used to create long range plasmophore rulers. Polythiophene (PTh) was chosen as the luminescent material for its well-defined emission in the visible spectrum [50]. For this study, the OWL method is critical as it allows one to tailor the dimensions of the metal segment and therefore its SPR wavelength (from visible to near-infrared), as well as the gap separating it from the luminescent polymer segment (Fig. 2.1 and Fig. 2.2). This control becomes the basis for the long range plasmophore rulers.

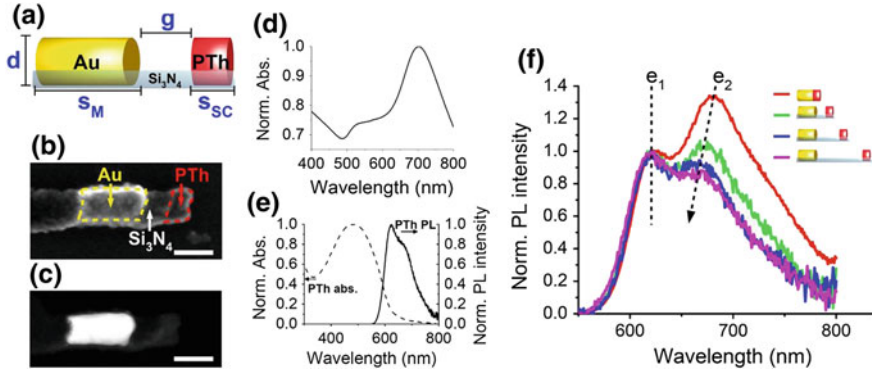


**Fig. 2.2** The long-range plasmophore ruler. **a** Schematic depiction of the plasmophore ruler designed via OWL, composed of a gold nanorod and a polythiophene (PTh) nanodisk. The silicon nitride backing acts as a rigid spacer holding the PTh disk at a fixed distance from the Au nanorod. Control over the Au and PTh segment lengths ( $s_M$  and  $s_{SC}$ , respectively), the diameter of the rods (**d**) and the gap length (**g**) is demonstrated. **(b, SEM)** and **(c, z-contrast STEM)** are electron microscopy images of the same hybrid structure composed of a Au nanorod and a PTh disk, whose dimensions ( $d = 40 \pm 7$  nm,  $s_M = 82 \pm 5$  nm and  $s_{SC} = 30 \pm 10$  nm) have been optimized to maximize the plasmophore ruler signal. The gap length of the structure shown in **b** and **c** is:  $g = 43 \pm 12$  nm. Scale bars in **b** and **c** are 50 nm. **d** Solution-phase normalized absorbance spectrum of the hybrid shown in **b** and **c**, with  $\lambda_{SPR} = 695$  nm. **e** Solution-phase normalized absorbance (dotted line, left axis) and PL (solid line, right axis) spectra of the pure PTh nanorods. **f** PL spectra of hybrids excited at 440 nm (same dimensions as the one shown in **b** and **c** but with different gap lengths) showing the distance dependence of the plasmonic modulation of the PTh emission (red curve no gap, green curve  $g = 43 \pm 12$  nm, blue curve  $g = 140 \pm 33$  nm, magenta curve  $g = 330 \pm 31$  nm) (Color figure online)

## 2.2 Results and Discussion

The modification of the PTh emission by plasmonic antennas was studied by measuring the solution-averaged PL of AuPTh nanorods (rod diameter:  $40 \pm 7$  nm, PTh disk length:  $30 \pm 10$  nm, no gap) with various gold segment lengths. The broad emission of the pure PTh corresponds to one electronic transition that has a maximum ( $e_1$ ) at  $\lambda_1 = 622$  nm and a shoulder ( $e_2$ ) around  $\lambda_2 = 660$  nm, and which overlaps well with the SPR of the Au rod (Fig. 2.2e). The Au rod SPR was varied from 600 to 840 nm, corresponding to gold nanorod lengths ranging from 52 to 123 nm (aspect ratios  $AR = \text{length/diameter}$  varied from 1.27 to 3.24). The position of the Au rod SPR strongly affects the shape of the PTh emission: it modifies the relative intensities of  $e_1$  ( $I_1$ ) and  $e_2$  ( $I_2$ ) and significantly shifts the position of  $\lambda_2$  (Figs. 2.3). To clearly observe this change, all of the PL spectra were normalized at  $e_1$ . We use the ratio  $R_{2/1} = I_2/I_1$  between the intensities of  $e_2$  and  $e_1$  to quantify the modulation of the PTh PL by the Au antenna.  $R_{2/1}$  increases for SPR ranging from 600 to 695 nm, and decreases as the SPR is further red-shifted from the PTh emission band (Fig. 2.4). When the SPR is centered at 695 nm (corresponding to a

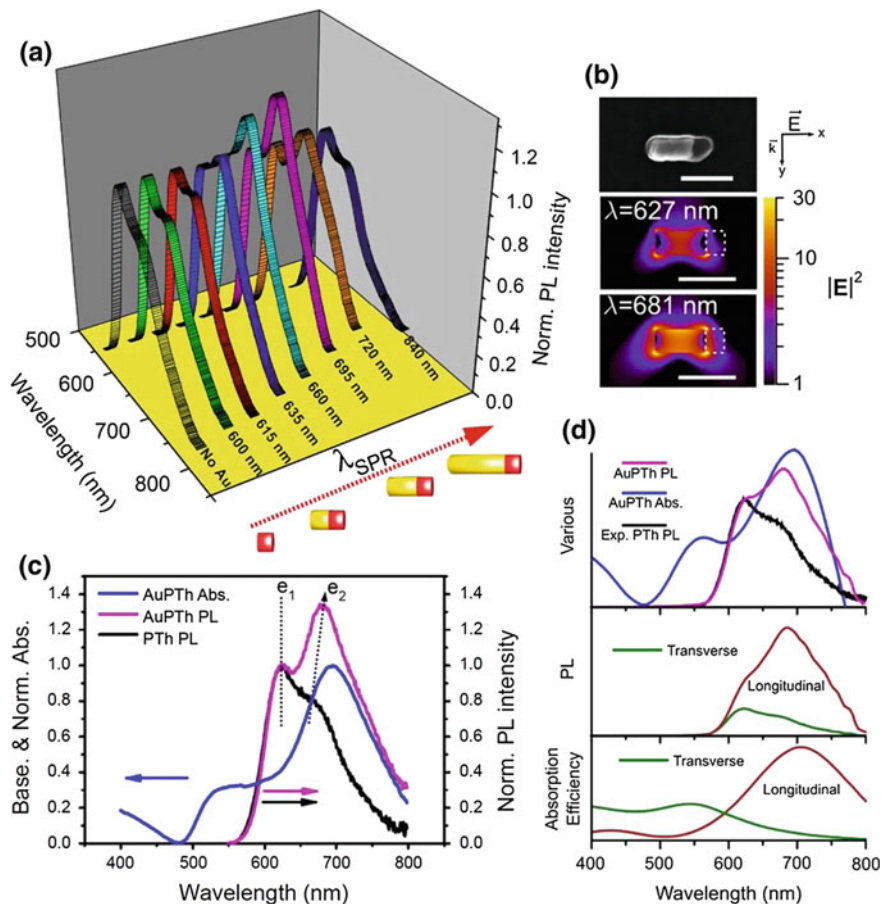


**Fig. 2.3** Modification of the polythiophene (PTh) PL by adjacent Au nanorods as a function of the SPR wavelength. **a** PL spectra of Au nanorod/PTh disk structures (no gap, rod diameter:  $40 \pm 7$  nm, PTh length:  $30 \pm 10$  nm) with various gold segment lengths in Nanopure™ water. Excitation wavelength: 440 nm. The curves were normalized to  $e_1$  ( $\lambda_1 = 624$  nm). The *black* curve corresponds to the pure PTh emission (no Au rod). As the Au length is increased (*curves from left to right*), the SPR red shifts (mentioned in *black* next to the PL curves) going from 600 to 840 nm. **b** *Top* SEM image of AuPTh hybrid—SPR centered at 695 nm corresponding to a Au rod length of 82 nm. *Bottom* electric field maps of the simulated AuPTh hybrid (Au rod length: 82 nm and diameter: 44 nm, PTh length: 30 nm), longitudinal polarization (along x axis). Scale bars: 100 nm. The difference in the strength of the electric field inside the PTh (*white dashed lines* in the field maps) between the *center* and *lower panels* indicates the difference in coupling strength between the gold and the PTh and is directly responsible for the increased emission at 681 nm as compared to 627 nm. **c** Overlap between the absorbance (*blue curve*) and the PL spectra (*magenta curve*, excitation wavelength: 440 nm) of a AuPTh hybrid (Au rod length: 82 nm)—SPR centered at 695 nm. The pure PTh PL spectrum is shown as a reference (*black curve*). The curves were base-lined and normalized for clarity. **d** DDA simulations of a AuPTh system similar to the experimental one shown in Fig. 2.3b and c. Length of the gold segment is 82 nm and the diameter is 44 nm. The length of the PTh segment is 30 nm. The simulated spectra (PL and absorbance, top graph) have been obtained by averaging the PL and the absorbance over three different E-field polarizations (along the three main axes)

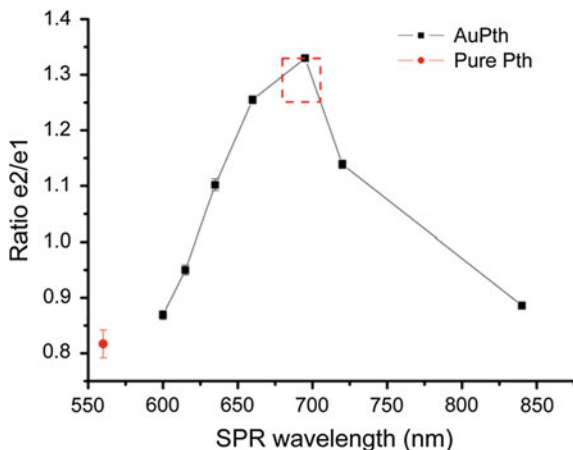


**Fig. 2.4** Ratio between the PL intensity at  $e_1$  and  $e_2$  of the AuPth nanorods as a function of the SPR wavelength. The red dotted rectangle highlights the region investigated with the Au/gap/Pth structures. The SPR of these hybrids was centered at  $695 \pm 15$  nm, corresponding to an initial value for AuPth nanorods (without a gap) of  $R_{2/1}$  comprised between 1.33 and 1.25. The y-error bars are due to the uncertainty in determining the ratio  $e_2/e_1$  (Color figure online)

Au rod length of 82 nm), the modification of the emission band shape is the highest. The position of the shoulder  $e_2$  shifts from 660 to 680 nm and  $R_{2/1}$  increases by 1.6 fold (going from  $\approx 0.82$  without the Au rod to  $\approx 1.33$ ).

The discrete dipole approximation (DDA) was used to model the AuPth nanorods (based on a reciprocity theorem analysis of the PL spectra where emission enhancement can be directly related to increased radiative rate) [51–53]. The AuPth hybrid having an experimental  $\lambda_{\text{SPR}} = 695$  nm (Au rod length:  $82 \pm 5$  nm and diameter:  $40 \pm 7$  nm, PTh length:  $30 \pm 10$  nm) was modeled with a AuPth structure having a theoretical  $\lambda_{\text{SPR}} = 695$  nm (Au rod length: 82 nm and diameter: 44 nm, PTh length: 30 nm). The simulated emission of this AuPth hybrid has  $\lambda_1 = 627$  nm and  $\lambda_2 = 681$  nm, which are close to the experimental values (i.e. 624 nm and 680 nm, respectively). DDA simulations show that when the Au rod SPR is centered at around 570 nm, the electric field strength integrated over the volume of the PTh is approximately 1.02 times larger at 627 nm than at 681 nm (Fig. 2.5). When the SPR band of the simulated AuPth rod is centered at 695 nm, it still overlaps with the PTh PL spectra and the electric field at 681 nm is 1.68 times higher than at 627 nm. In this case,  $R_{2/1}$  increases by 1.76 fold due to the presence of the gold rod, which is similar to our experimental data (i.e.  $R_{2/1}$  increases by 1.6 fold for  $\lambda_{\text{SPR}} = 695$  nm). This minor discrepancy between the experimental and theoretical peak ratios may be explained by very small differences in quenching between the  $e_1$  and  $e_2$  band. Overall, quenching is expected to be low due to the large spatial extent of the electric field outside the nanoparticle, as quenching is usually only substantive within several nm of the metal surface. Recent experiments on a similar system, poly(3-hexylthiophene), have shown that



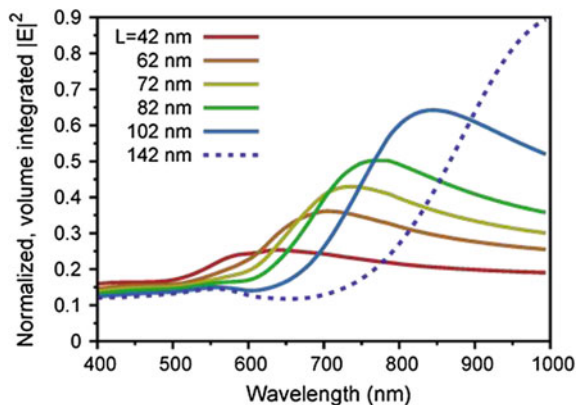


**Fig. 2.5** DDA simulation of the effect of increasing the length of the gold segment (diameter: 44 nm) on the volume integrated electric field strength inside the PTh (PTh segment diameter: 44 nm and length: 30 nm). Note that the difference in intensity for the AR = 0.95 (Au length = 42 nm) nanorod ( $\lambda_{\text{SPR}} = 570$  nm) between 627 nm (the approximate location of  $e_1$ ) and 681 nm (the approximate location of  $e_2$ ) is negligible, whereas for AR = 1.86 (Au length = 82 nm) case ( $\lambda_{\text{SPR}} = 695$  nm), the volume integrated field strength increases dramatically between  $e_1$  and  $e_2$ . When the LSPR shifts past 695 nm, the difference in field strength between  $e_1$  and  $e_2$  reduces and  $R_{2/1}$  reduces (see Fig. 2.4)

essentially no quenching occurs at gold-dye distances above 10 nm [29]. As the SPR shifts further to the red, the peak electric field strength increases (Fig. 2.5), but the overlap between the electric field enhancement and the PL spectrum reduces leading to a decrease of  $R_{2/1}$ . Contours of the local field at  $\lambda_1$  (627 nm) and  $\lambda_2$  (681 nm) for simulated structures with a gold rod length of 82 nm ( $\lambda_{\text{SPR}} = 695$  nm) are presented in Fig. 2.3b, while Fig. 2.3d shows modeled DDA PL and absorbance spectra analogous to the experimental results in Fig. 2.3c, as well as the breakdown of the spectra into longitudinal and transverse components. The calculations are in quantitative agreement with experiments. Therefore, the plasmonic modulation of AuPTh nanorod PL depends on: (i) the relative value of  $I_2$  and  $I_1$  (i.e.  $R_{2/1}$ ) without the Au rod and (ii) the difference in the electric field within the PTh segment at  $\lambda_2$  and  $\lambda_1$  (directly related to the spectral overlap between the SPR band and the pure PTh PL spectrum). Recent experiments have demonstrated PL emission from pure nanorods that follows the far-field scattering pattern of the longitudinal nanorod SPR upon irradiation of either the transverse SPR, the interband transitions, or the longitudinal SPR itself [54]. However, the quantum yield of the nanorod emission is around  $2 \times 10^{-6}$  which is four orders of magnitude lower than the quantum yield of the emission of polythiophene systems, typically around  $10^{-2}$ – $10^{-1}$  [55]. We did not observe any measurable PL from the pure Au nanorod solutions, and as such the Au nanorod does not contribute significantly to the PL spectrum.

With OWL, we can study the long-range validity of this novel plasmophore ruler by introducing a gap between the Au nanorod and the PTh segment. We use this technique to create billions of highly monodisperse rods and obtain statistically

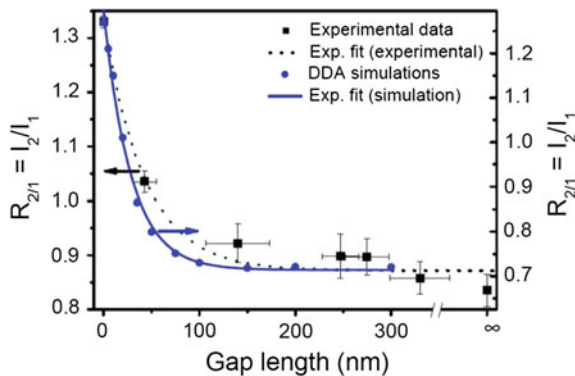


**Fig. 2.6** Effect of the gap length on the plasmonic modulation of the polythiophene (PTh) PL. *Black squares (left axis)*: plot of measured  $R_{2/1} = I_2/I_1$  as a function of the gap length, where  $I_1$  and  $I_2$  are the PL intensities at  $e_1$  and  $e_2$ , respectively. The Au rod/gap/PTh disk hybrids used for these measurements had a SPR wavelength centered at  $695 \pm 15$  nm. The diameter of the whole structure was  $40 \pm 7$  nm. The Au nanorod was  $82 \pm 5$  nm long and the PTh disk was  $30 \pm 10$  nm long. Each data point corresponds to one solution of nanorods (i.e. one set of structures). The x-error bars are the standard deviations of the gap lengths based on TEM measurements (more than 150 rods were measured for each sample). The y-error bars are due to the uncertainty in determining  $R_{2/1}$  from the PL curves. The *dotted black line* is a guide for the eye and corresponds to an exponential decay fit. The point at  $x = \infty$  corresponds to the pure PTh case (no Au rod). *Blue circles (right axis)*: DDA simulations of  $R_{2/1}$  for a Au/PTh system having similar absorbance and PL as the experimental one shown in Fig. 2.3c. The Au segment is 82 nm long, and both the gold and the PTh have a diameter of 44 nm. The length of the PTh segment is 30 nm. The *solid blue curve* is a guide to the eyes and corresponds to an exponential decay fit. The data plots (experimental and simulation) are fit to a single-exponential decay of the form  $R_{2/1} = a \cdot \exp(-g/\tau) + b$ , where  $g$  is the gap length. Experimental data:  $a = 0.46 \pm 0.02$ ,  $\tau = 42.7 \pm 6.0$ ,  $b = 0.87 \pm 0.02$ . DDA simulations:  $a = 0.58 \pm 0.01$ ,  $\tau = 28.4 \pm 1.8$ ,  $b = 0.71 \pm 0.01$  (Color figure online)

significant data by doing solution-phase measurements that are ensemble-averaged (the sample volume was 500  $\mu\text{L}$  and the concentration of nanostructures was estimated to be in the high picomolar concentration range).

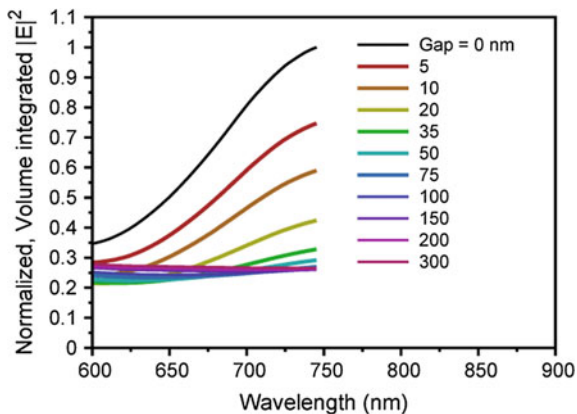
To maximize the plasmonic modulation of the PTh PL, we studied Au nanorod/gap/PTh nanodisk dimers having a SPR centered at  $695 \pm 15$  nm (rod diameter:  $40 \pm 7$  nm, Au length:  $82 \pm 5$  nm, and PTh length:  $30 \pm 10$  nm). The effect of the Au antenna on the PTh emission decreases as the PTh disk is located further away from the Au rod (Fig. 2.2f). This is clearly observed when one examined the dependence of  $R_{2/1}$  on the gap size, which can be fitted with a single-exponential decay of the form

$$R_{2/1} = a \cdot \exp(-g/\tau) + b \quad (2.1)$$

with  $\tau = 42.7 \pm 6.0$ , where  $g$  is the gap length (Fig. 2.6, black dotted line). DDA simulations agree well with experimental data (Fig. 2.6, blue circles), with a decay constant  $\tau = 28.4 \pm 1.8$ . A long-range interaction, which becomes negligible above



**Fig. 2.7** DDA simulation of the effect of increasing the gap between the gold (diameter: 44 nm, length: 82 nm) and the PTh (diameter: 44 nm, length: 30 nm) on the volume integrated electric field strength inside the PTh. There is a 60 % reduction in the field strength when the gap is increased from 0 nm to 20 nm



100 nm, is observed. The electric field at the end of the Au nanorod (longitudinal polarization) decays over a similar length scale (Fig. 2.3b and 2.7).

FDTD simulations performed by Ming et al. suggest that the PL polarization of a fluorophore located at the end of a gold nanorod follows a similar distance dependence (Au rod diameter: 30 nm and length: 70 nm) [31]. This result, coupled with our experimental and theoretical data (Fig. 2.6), suggests that the decay of the electric field intensity away from the Au nanorod accounts for the decrease of  $R_{2/1}$  as the gap becomes larger, with nearly 60 % of the reduction in the volume integrated electric field at 695 nm occurring when the gap increases from 0 to 20 nm (Fig. 2.7). By measuring  $R_{2/1}$  for a specific fluorophore/plasmonic structure pair, we therefore can determine the distance between the two constructs, similar to the plasmon ruler which provides a measure of the distance between two plasmonic nanostructures [7, 10, 12, 56–58]. Comparison with previous works suggests that the plasmophore ruler presented in this manuscript has a longer range (relative to the nanostructure dimensions) than plasmon rulers based on Au NP dimers [10].

## 2.3 Conclusions

This work shows how the distance between well-defined plasmonic nanostructures and fluorescent entities can be used to modulate the emission shape of a particular plasmophore. That dependence constitutes a new type of long-range ruler that allows one to probe distances on the 0–100 nm length scale, independently on the signal intensity. A new theory has been developed to describe the results, and it confirms the electromagnetic origin of the dependence of the spectral lineshape on plasmophore structural parameters. It should be noted that these are a proof-of-concept results that provide valuable information for designing more functional rulers, such as the ones used for in vivo studies, where a reference signal cannot practically be incorporated [12].

## 2.4 Methods and Materials

### 2.4.1 *Materials and Instruments*

All chemicals and solutions were used as received. The plating solutions named Cyless, Orotemp 24 Rack and nickel sulfamate were purchased from Technic, Inc. The anodized aluminum oxide (AAO) membranes used for the nanowire synthesis were purchased from Synkera Technologies, Inc. with nominal pore diameters of 35, 55, and 73 nm. The membranes used for filtration were purchased from Whatman (0.2  $\mu\text{m}$  Anodisc 47 membranes). Thiophene ( $\geq 99\%$ ), boron trifluoride diethyl etherate and sodium citrate were purchased from Sigma. Nanopure™ water was used.

SEM and z-contrast STEM images were acquired using a Hitachi S-4800 and a Hitachi HD-2300, respectively. Extinction spectra were collected in aqueous solutions using quartz cuvettes (1 cm path length) and a Varian Cary 5000 UV-Vis-NIR spectrophotometer. Fluorescence spectra were collected in aqueous solution using quartz cuvettes (1 cm path length) and a HORIBA Jobin Yvon FluoroLog-3 with excitation and emission slits of 5 nm. Silicon nitride backings were deposited using an AJA Orion Sputter. Electrochemical deposition was done using an EC epsilon potentiostat (BASinc) with a classic three-electrode electrochemical cell. Platinum foil was used as the counter electrode (CE) and the reference electrode was a Ag/AgCl electrode.

### 2.4.2 *Nanowire Synthesis*

The nanowires were electrochemically synthesized within AAO membranes (Synkera, Inc.). The general method for producing OWL nanowires made of metal is described in our previous publications [41, 42]. Briefly, 200 nm of silver was thermally evaporated on one side of the AAO templates for electrical connection. Silver was deposited at  $-940\text{ mV}$  (vs Ag/AgCl) using Cyless plating solution (Technic, Inc.), Au was deposited at  $-1100\text{ mV}$  (vs Ag/AgCl) using concentrated Orotemp 24 Rack plating solution (Technic, Inc.), and Ni was deposited at  $-1100\text{ mV}$  (vs Ag/AgCl) using nickel sulfamate plating solution (Technic, Inc.). Prior to the wire synthesis, the pores of the AAO templates were filled with 1000 mC of silver, followed by 250 mC of nickel. These sacrificial segments are necessary to ensure that the nanowire segments of interest are deposited in more uniform and less branched part of the AAO template.

Polythiophene nanorods were grown with a two electrode set-up using a platinum counter electrode (CE), similarly to the synthesis of poly(3-hexylthiophene) nanorods reported by O'Carroll et al. [26, 29]. Prior to the deposition, the cell and the CE were immersed in isopropyl alcohol (IPA), dried under  $\text{N}_2$  and under vacuum to remove any residual water. 50  $\mu\text{L}$  of thiophene monomer were dissolved

in 5 mL of boron trifluoride diethyl-etherate (BFEE) and deposited with 0.02 s pulses at +3 V, followed by 5 s pulses at −600 mV. The template was successively rinsed with acetonitrile and IPA, and was dried with N<sub>2</sub>.

The silver backing was dissolved in a 4:1:1 ethanol: ammonium hydroxide: hydrogen peroxide solution during 20 min. The template was then rinsed thoroughly in H<sub>2</sub>O. The AAO template was dissolved in 2 M NaOH (0.5 % citrate by weight) aqueous solution (one hour). The nanowires were recovered using centrifugation (4000 RPM 5 min), and were washed four times with 0.1 % (by weight) citrate aqueous solution. The wires were then dispersed in 24 mL of 0.1 % aqueous citrate solution using sonication before being vacuum filtered onto 47 mm AAO membranes (0.2 μm pores, from Whatman, 2 mL/membrane). A total of twelve membranes were used per nanorod batch in order to avoid aggregation at the surface of the membrane during the filtration process. The membranes were left to dry in air before being sputter coated with a thin layer of silicon nitride (support layer for holding plasmonic Au segment and fluorescent polymer segment after sacrificial Ni segment removal). Radio frequency sputtering plasma was initiated at 40 mTorr pressure and the deposition proceeded at 5 mTorr. The sputtering time was 4 min 15 s, 5 min and 5 min 30 s for nanorods with nominal diameters of 35, 55 and 73 nm respectively. The carrier gas was argon, and the power used was 150 W. To recover the rods coated with Si<sub>3</sub>N<sub>4</sub>, 20 mL of 3 M NaOH, followed by 100 mL of H<sub>2</sub>O, were vacuum filtered through the AAO templates to minimize the interaction between the nanowires and the AAO surface. The nanorods were recovered back into solution by sonicating each of the nanowire-coated AAO membranes in H<sub>2</sub>O (10 mL, 0.1 % citrate) for 30 s. 2 mL of 0.5 M NaOH and 0.1 % citrate aqueous solution were then added to the released nanorods in order to dissolve the residual AAO. The solution was left 5 min before being centrifuged at 4000 RPM for 10 min. The rods were then washed with H<sub>2</sub>O (0.1 % citrate) and centrifuged at 4000 RPM for 5 min three times. The rods were dispersed in 500 μL of H<sub>2</sub>O (0.1 % citrate) and etched for 2 h in 5 % H<sub>3</sub>PO<sub>4</sub>. Finally they were centrifuged twice and dispersed in 500 μL of H<sub>2</sub>O (0.1 % citrate) before any further optical or material characterization.

### 2.4.3 Discrete Dipole Approximation Simulations

The discrete dipole approximation (DDA) [51, 52] was used to estimate the coupling between the emission of the PTh and the near field of the gold using a model based on the reciprocity theorem [59] in which the time reverse of the PL process is modeled to determine the PTh optical constants that are needed in a DDA calculation of the interaction of a plane wave field with the gold rod/PTh structure. The enhanced fields in the polymer from the DDA calculation are then used to determine the plasmon enhanced PL spectrum using the PTh optical constants.

To implement this theory, the PL spectrum of PTh was modeled as a direct absorption process by relating the emission profile to the imaginary part of the dielectric function

$$\varepsilon(\omega) = \varepsilon_{\text{Re}}(\omega) + i\varepsilon_{\text{Im}}(\omega) \quad (2.2)$$

of an artificial material via

$$\varepsilon_{\text{Im}}(\omega) = \alpha I_{\text{PL}}/\omega^3 \quad (2.3)$$

where  $I_{\text{PL}}$  is the normalized PL intensity of the PTh,  $\omega$  is the outgoing photon frequency, and  $\alpha$  is an artificial constant that is determined via an empirical fit to the experimental results (here,  $\alpha = 3.0 \text{ eV}^3$ ). The term  $\omega^3$  is included to remove the intrinsic frequency dependence of the PL spectrum (which is related to the Einstein “A” coefficient) [60] such that  $\varepsilon_{\text{Im}}$  is directly proportional to the square of the transition dipole matrix elements of the emitter.

The real part of the polymer dielectric function is determined by fitting  $\varepsilon_{\text{Im}}$  to a sum of oscillators:

$$\varepsilon_{\text{Im}}(\omega) = \text{Im} \left( 1 + \sum_i \frac{a}{\omega_i^2 - \omega^2 - i\gamma\omega} \right) \quad (2.4)$$

and taking the real part of the resulting fit (which is a version of a Kramers-Kronig transformation). The gold was modeled using the optical constants of Johnson and Christy [61], with corrections for surface scattering, surface anomalies and polycrystallinity of the OWL structures. The effective electron mean free path was reduced to 10 nm in the simulations [62].

Once the polymer and gold dielectric functions are known, a DDA calculation is used to determine the plasmon-enhanced local field  $\mathbf{E}$  inside the polymer. The plasmon enhanced PL rate is then given by [63]

$$Q_{\text{PL}}(\omega) = \int_{\text{PTh}} \omega^3 \varepsilon_{\text{Im}}^{\text{PTh}} |\mathbf{E}|^2 dV \quad (2.5)$$

where there is a multiplicative  $\omega^2$  (in addition the original  $\omega$  in the Landau and Lifshitz derivation) to account for the fact that this is a spontaneous emission process. This allows us to relate the rate of energy loss via single particle transitions directly to the creation of photons. Note that the use of  $|\mathbf{E}|^2$  associated with a plane wave source in the local field calculation is equivalent to the well-known plane-wave approximation in the SERS enhancement factor calculations [64] and is justified based on a reciprocity theorem analysis as described by Kerker [59]. While the plane wave approximation works best in the quasistatic (small particle) limit, the error will be minor for the particle sizes being considered here due to the rapid decay of  $|\mathbf{E}|^2$  within the polymer with distance from the gold surface. Also, it is

likely that PL is quenched in the polymer for the first few nm from the gold surface due to electron transfer or other relaxation processes, but this is neglected in the present analysis as a secondary effect as the spatial extent of the enhanced fields is much larger than this quenching region.

## References

1. Stryer, L., & Haugland, R. P. (1967). FRET paper. *PNAS*, 58, 719–725.
2. Weiss, S. (1999). Fluorescence spectroscopy of single biomolecules. *Science*, 283, 1676.
3. Singh, A. K., Khan, S. A., Fan, Z., Demeritte, T., Senapati, D., Kanchanapally, R., et al. (2012). Development of a long-range surface-enhanced Raman spectroscopy ruler. *Journal of the American Chemical Society*, 134, 8662.
4. Yun, C. S., Javier, A., Jennings, T., Fisher, M., Hira, S., Peterson, S., et al. (2005). Nanometal surface energy transfer in optical rulers, breaking the FRET barrier. *Journal of the American Chemical Society*, 127, 3115.
5. Dulkeith, E., Ringler, M., Klar, T. A., & Feldmann, J. (2005). Gold Nanoparticles Quench Fluorescence by Phase Induced Radiative Rate Suppression. *Nano Letters*, 5, 585.
6. Seelig, J., Leslie, K., Renn, A., Kuhn, S., Jacobsen, V., Corput, M. V. D., et al. (2007). Nanoparticle-induced fluorescence lifetime modification as nanoscopic ruler: demonstration at the single molecule level. *Nano Letters*, 7, 685.
7. Reinhard, B. M., Siu, M., Agarwal, H., Alivisatos, A. P., & Liphardt, J. (2005). Calibration of dynamic molecular rulers based on plasmon coupling between gold nanoparticles. *Nano Letters*, 5, 2246.
8. Sonnichsen, C., Reinhard, B. M., Liphardt, J., & Alivisatos, A. P. (2005). A molecular ruler based on plasmon coupling of single gold and silver nanoparticles. *Nature Biotechnology*, 23, 741.
9. Liu, G. L., Yin, Y., Kunchakarra, S., Mukherjee, B., Gerion, D., Jett, S. D., et al. (2006). A nanoplasmonic molecular ruler for measuring nuclease activity and DNA footprinting. *Nature Nanotechnology*, 1, 47.
10. Jain, P. K., Huang, W., & El-Sayed, M. A. (2007). On the universal scaling behavior of the distance decay of plasmon coupling in metal nanoparticle pairs: a plasmon ruler equation. *Nano Letters*, 7, 2080.
11. Reinhard, B. M., Sheikholeslami, S., Mastroianni, A., Alivisatos, A. P., & Liphardt, J. (2007). Use of plasmon coupling to reveal the dynamics of DNA bending and cleavage by single EcoRV restriction enzymes. *PNAS*, 104, 2667.
12. Jun, Y.-W., Sheikholeslami, S., Hostetter, D. R., Tajon, C., Craik, C. S., & Alivisatos, A. P. (2009). Continuous imaging of plasmon rulers in live cells reveals early-stage caspase-3 activation at the single-molecule level. *PNAS*, 106, 17735.
13. Liu, N., Hentschel, M., Weiss, T., Alivisatos, A. P., & Giessen, H. (2011). Three-dimensional plasmon rulers. *Science*, 332, 1407.
14. Lakowicz, J. R., Ray, K., Chowdhury, M., Szmajcinski, H., Fu, Y., Zhang, J., et al. (2008). Plasmon-controlled fluorescence: a new paradigm in fluorescence spectroscopy. *The Analyst*, 133, 1308.
15. Kim, B.-H., Cho, C.-H., Mun, J.-S., Kwon, M.-K., Park, T.-Y., Kim, J. S., et al. (2008). Enhancement of the external quantum efficiency of a silicon quantum dot light-emitting diode by localized surface plasmons. *Advanced Materials*, 20, 3100.
16. Schuller, J. A., Barnard, E. S., Cai, W., Jun, Y. C., & White, J. (2010). Plasmonics for extreme light concentration and manipulation. *Nature Materials*, 9, 193.
17. Ferry, V. E., Munday, J. N., & Atwater, H. A. (2010). Design considerations for plasmonic photovoltaics. *Advanced Materials*, 22, 4794.

18. Mubeen, S., Hernandez-Sosa, G., Moses, D., Lee, J., & Moskovits, M. (2011). Plasmonic photosensitization of a wide band gap semiconductor: converting plasmons to charge carriers. *Nano Letters*, *11*, 5548.
19. Linic, S., Christopher, P., & Ingram, D. B. (2011). Plasmonic-metal nanostructures for efficient conversion of solar to chemical energy. *Nature Materials*, *10*, 911.
20. Christopher, P., Xin, H., & Linic, S. (2011). Visible-light-enhanced catalytic oxidation reactions on plasmonic silver nanostructures. *Nature Chemistry*, *3*, 467.
21. Lee, J., Mubeen, S., Ji, X., Stucky, G. D., & Moskovits, M. (2012). Plasmonic photoanodes for solar water splitting with visible light. *Nano Letters*, *12*, 5014.
22. Neretina, S., Qian, W., Dreaden, E. C., & El-Sayed, M. A. (2009). Exciton lifetime tuning by changing the plasmon field orientation with respect to the exciton transition moment direction: CdTe-Au core-shell nanorods. *Nano Letters*, *9*, 1242.
23. Wang, Y., Yang, T., Tuominen, M. T., & Aichermann, M. (2009). Radiative rate enhancements in ensembles of hybrid metal-semiconductor nanostructures. *Physical Review Letters*, *102*, 163001.
24. Pompa, P. P., Martiradonna, L., Torre, A. D., Sala, F. D., Manna, L., Vittorio, M. D., et al. (2006). Metal-enhanced fluorescence of colloidal nanocrystals with nanoscale control. *Nature Nanotechnology*, *1*, 126.
25. Singh, M. P., & Strouse, G. F. (2010). Involvement of the LSPR spectral overlap for energy transfer between a dye and Au nanoparticle. *Journal of the American Chemical Society*, *132*, 9383.
26. O'Carroll, D. M., Fakonas, J. S., Callahan, D. M., Schierhorn, M., & Atwater, H. A. (2012). Metal-polymer-metal split-dipole nanoantennas. *Advanced Materials*, *24*(OP13), 6.
27. Taminiau, T. H., Stefani, F. D., Segerink, F. B., & Hulst, N. F. V. (2008). Optical antennas direct single-molecule emission. *Nature Photonics*, *2*, 234.
28. Ming, T., Zhao, L., Yang, Z., Chen, H., Sun, L., Wang, J., et al. (2009). Strong polarization dependence of plasmon-enhanced fluorescence on single gold nanorods. *Nano Letters*, *9*, 3896.
29. O'Carroll, D. M., Hofmann, C. E., & Atwater, H. A. (2010). Conjugated polymer/metal nanowire heterostructure plasmonic antennas. *Advanced Materials*, *22*, 1223.
30. Ozel, T., Nizamoglu, S., Sefunc, M. A., Samarskaya, O., Ozel, I. O., Mutlugun, E., et al. (2011). Anisotropic emission from multilayered plasmon resonator nanocomposites of isotropic semiconductor quantum dots. *ACS Nano*, *5*, 1328.
31. Ming, T., Zhao, L., Chen, H., Woo, K. C., Wang, J., & Lin, H.-Q. (2011). Experimental evidence of plasmaphores: plasmon-directed polarized emission from gold nanorod-fluorophore hybrid nanostructures. *Nano Letters*, *11*, 2296.
32. Cohen-Hoshen, E., Bryant, G. W., Pinkas, I., Sperling, J., & Bar-Joseph, I. (2012). Exciton-plasmon interaction in quantum dot gold nanoparticle structures. *Nano Letters*, *12*, 4260.
33. Kottmann, P. K., Martin, O. J. F., Smith, D. R., Schultz, S. (2000). Spectral response of plasmon resonant nanoparticles with a non-regular shape. *Optics Express*, *6*, 213.
34. Ringler, M., Schwemer, A., Wunderlich, M., Nichtl, A., Kurzinger, K., Klar, T. A., et al. (2008). Shaping emission of fluorescent molecules with single plasmonic nanoresonators. *Physical Review Letters*, *100*, 203002.
35. Ozel, T., Soganci, I. M., Nizamoglu, S., Huyal, I. O., Mutlugun, E., Sapra, S., et al. (2008). Selective enhancement of surface-state emission and simultaneous quenching of interband transition in white-luminophor CdS nanocrystals using localized plasmon coupling. *New Journal of Physics*, *10*, 083035.
36. Zhao, L., Ming, T., Chen, H., Liang, Y., & Wang, J. (2011). Plasmon-induced modulation of the emission spectra of the fluorescent molecules near gold nanorods. *Nanoscale*, *3*, 3849.
37. Yun, C. S., Javier, A., Jennings, T., Fisher, M., Hira, S., Peterson, S., et al. (2005). Nanometal surface energy transfer in optical rulers, breaking the FRET barrier. *Journal of the American Chemical Society*, *127*, 3115.
38. Qin, L., Park, S., Huang, L., & Mirkin, C. A. (2005). On-wire lithography. *Science*, *309*, 113.

39. Qin, L., Jang, J. W., Huang, L., & Mirkin, C. A. (2007). Sub-5-nm gaps prepared by on-wire lithography: correlating gap size with electrical transport. *Small (Weinheim an der Bergstrasse, Germany)*, 3, 86.
40. Banholzer, M. J., Li, S., Ketter, J. B., Rozkiewicz, D. I., Schatz, G. C., & Mirkin, C. A. (2008). An electrochemical approach to and the physical consequences of preparing nanostructures from gold nanorods with smooth ends. *The Journal of physical chemistry. C, Nanomaterials and interfaces*, 112, 15729.
41. Banholzer, M. J., Qin, L., Millstone, J. E., Osberg, K. D., & Mirkin, C. A. (2009). On-wire lithography: synthesis, encoding and biological applications. *Nature Protocols*, 4, 838.
42. Osberg, K. D., Schmucker, A. L., Senesi, A. J., & Mirkin, C. A. (2011). One-dimensional nanorod arrays: independent control of composition, length, and interparticle spacing with nanometer precision. *Nano Letters*, 11, 820.
43. Gunnarsson, L., Rindzevicius, T., Prikulis, J., Kasemo, B., Kall, M., Zou, S., et al. (1979). Confined plasmons in nanofabricated single silver particle pairs: experimental observations of strong interparticle interactions. *The Journal of Physical Chemistry B*, 2005, 109.
44. Chen, X., Jeon, Y.-M., Jang, J.-W., Qin, L., Huo, F., Wei, W., et al. (2008). Plasmonic focusing in rod-sheath heteronanostructures. *Journal of the American Chemical Society*, 130, 8166.
45. Schmucker, A. L., Barin, G., Brown, K. A., Rycenga, M., Coskun, A., Buyukcikir, O., et al. (2012). Electronic and optical vibrational spectroscopy of molecular transport junctions created by on-wire lithography. *Small*, 9, 1900.
46. Lidong, Q., Shengli, Z., Can, X., Ariel, A. C. S. G., & Mirkin, C. A. (2006). Designing, fabricating, and imaging raman hot spots. *PNAS*, 103, 13300.
47. Qin, L., Banholzer, M. J., Millstone, J. E., & Mirkin, C. A. (2007). Nanodisk codes. *Nano Letters*, 7, 3849.
48. Osberg, K. D., Rycenga, M., Bourret, G. R., Brown, K. A., & Mirkin, C. A. (2012). Dispersible surface-enhanced raman scattering nanosheets. *Advanced Materials*, 24, 6065 doi:10.1002/adma.201202845.
49. Osberg, K. D., Rycenga, M., Harris, N., Schmucker, A. L., Langille, M. R., Schatz, G. C., et al. (2012). Dispersible gold nanorod dimers with sub-5nm gaps as local amplifiers for surface-enhanced raman scattering. *Nano Letters*, 12, 3828.
50. Vardeny, Z., Ehrenfreund, E., Brafman, O., Nowak, M., Schaffer, H., Heeger, A., et al. (1986). Photogeneration of confined soliton pairs (bipolarons) in polythiophene. *Physical Review Letters*, 56, 671.
51. Draine, B. T., & Flatau, P. J. (1994). Discrete-dipole approximation for scattering calculations. *Journal of the Optical Society of America A*, 11, 1491.
52. Draine, B. T., & Flatau, P. J. (2012). User guide for the discrete dipole approximation code DDSCAT 7.2. [arXiv:1202.3424](https://arxiv.org/abs/1202.3424) [physics.comp-ph] 2012.
53. Flatau, P. J., & Draine, B. T. (2012). Fast near field calculations in the discrete dipole approximation for regular rectilinear grids. *Optics Express*, 20, 1247.
54. Fang, Y., Chang, W.-S., Willingham, B., Swanglap, P., Dominguez-Medina, S., & Link, S. (2012). Plasmon emission quantum yield of single gold nanorods as a function of aspect ratio. *ACS Nano*, 6, 7177.
55. Perepichka, I. F., Perepichka, D. F., Meng, H., & Wudl, F. (2005). Light-emitting polythiophenes. *Advanced Materials*, 17, 2281.
56. Sonnichsen, C., Reinhard, B. M., Liphardt, J., & Alivisatos, A. P. (2005). A molecular ruler based on plasmon coupling of single gold and silver nanoparticles. *Nature Biotechnology*, 23, 741.
57. Liu, G. L., Yin, Y., Kunchakarra, S., Mukherjee, B., Gerion, D., Jett, S. D., et al. (2006). A Nanoplasmonic molecular ruler for measuring nuclease activity and DNA footprinting. *Nature Nanotechnology*, 1, 47.
58. Liu, N., Hentschel, M., Weiss, T., Alivisatos, A. P., & Giessen, H. (2011). Three-dimensional plasmon rulers. *Science*, 332, 1407.



59. Kerker, M. (1969). *The scattering of light and other electromagnetic radiation*. New York: Academic Press.
60. Schatz, G. C., & Ratner, M. A. (2002). *Quantum mechanics in chemistry*; Courier Dover Publications, 2002.
61. Johnson, P. B., & Christy, R. W. (1972). Optical constants of the noble metals. *Physical Review B*, 6, 4370.
62. Kreibig, U., & Frangstein, C. v. (1969). The limitation of electron mean free path in small silver particles. *Zeitschrift für Physik*, 224, 307.
63. Landau, L. D., Bell, J., Kearsley, M., Pitaevskii, L., Lifshitz, E., & Sykes, J. (1984). *Electrodynamics of continuous media* (Vol. 8). Amsterdam: Elsevier.
64. Ausman, L. K., & Schatz, G. C. (2009). On the importance of incorporating dipole reradiation in the modeling of surface enhanced Raman scattering from spheres. *The Journal of Chemical Physics*, 131, 084708.

Coaxial Lithography

Ozel, T.

2016, XXIX, 92 p. 53 illus., 4 illus. in color., Hardcover

ISBN: 978-3-319-45413-9